

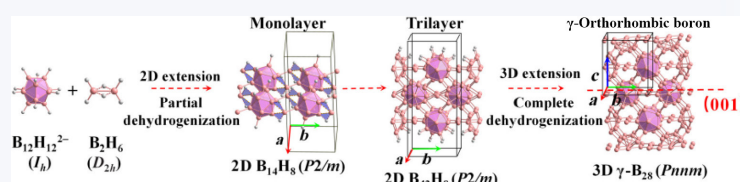
# Bottom-up approaches to form superatom-assembled 2D few-layered borophanes and carborophanes and 3D $\alpha$ -B<sub>12</sub>, $\gamma$ -B<sub>28</sub>, and B<sub>4</sub>C based on icosahedral B<sub>12</sub> and CB<sub>11</sub>

Qiao-Qiao Yan, Wen-Yan Zan, Yue-Wen Mu, and Si-Dian Li  

Institute of Molecular Science, Shanxi University, Taiyuan 030006, China

 Cite this article: *Nano Research*, 2025, 18, 94907288. <https://doi.org/10.26599/NR.2025.94907288>

**ABSTRACT:** Using the experimentally known aromatic icosahedral  $I_h$  B<sub>12</sub>H<sub>12</sub><sup>2-</sup> and C<sub>5v</sub> B<sub>11</sub>CH<sub>12</sub><sup>-</sup> as building blocks and based on extensive density functional theory calculations, we present herein bottom-up approaches to form the superatom-assembled two-dimensional (2D) few-layered  $\alpha$ -rhombohedral borophanes (B<sub>12</sub>)<sub>n</sub>H<sub>6</sub> ( $\alpha$ -1–5) and (B<sub>12</sub>)<sub>n</sub>H<sub>2</sub> ( $\alpha$ -6–10),  $\gamma$ -orthorhombic borophanes (B<sub>12</sub>-B<sub>2</sub>)<sub>n</sub>H<sub>8</sub> ( $\gamma$ -1–5), and carborophanes (CB<sub>11</sub>-CBC)<sub>n</sub>H<sub>8</sub> ( $\sigma$ -1–5) ( $n = 1–5$ ) and experimentally known three-dimensional (3D)  $\alpha$ -B<sub>12</sub>,  $\gamma$ -B<sub>28</sub>, and B<sub>4</sub>C crystals based on aromatic icosahedral B<sub>12</sub> and CB<sub>11</sub>, with the B–B dumbbells in  $\gamma$ -1–5 and C–B–C chains in  $\sigma$ -1–5 serving as interstitial units to help stabilize the systems. As both chemically and mechanically stable species, the optimized 2D monolayer, bilayer, trilayer, tetralayer, and pentalayer borophanes and carborophanes all turn out to be semiconductors in nature, in particular, the few-layered carborophanes  $\sigma$ -3–5 ((CB<sub>11</sub>-CBC)<sub>n</sub>H<sub>8</sub> ( $n = 3–5$ )) with the calculated band gaps of  $E_{\text{gap}} = 1.32–1.26$  eV appear to be well compatible with traditional silicon semiconductors in band gaps. Detailed adaptive natural density partitioning (AdNDP) bonding analyses indicate that both the icosahedral B<sub>12</sub> and CB<sub>11</sub> cages in these 2D and 3D crystal structures follow the universal superatomic electronic configuration of 1S<sup>2</sup>1P<sup>6</sup>1D<sup>10</sup>1F<sup>8</sup> matching the  $n + 1$  Wade's rule ( $n = 12$ ), rendering local spherical aromaticity and overall high stability to the systems.



**KEYWORDS:** boron nanomaterials, bottom-up approaches, density functional theory, Wade's rule, borophanes, carborophanes

## 1 Introduction

As a prototypical electron-deficient element in the periodic table, boron features multi-center-two-electron ( $mc$ -2e) bonding in both polyhedral molecules and crystal allotropes [1–3]. The aromatic icosahedral  $I_h$  B<sub>12</sub>H<sub>12</sub><sup>2-</sup>, C<sub>5v</sub> CB<sub>11</sub>H<sub>12</sub><sup>-</sup>, and  $D_{5d}$  1,12-C<sub>2</sub>B<sub>10</sub>H<sub>12</sub>, which all follow the  $n + 1$  Wade's rule ( $n = 12$ ) in the electronic configuration of 1S<sup>2</sup>1P<sup>6</sup>1D<sup>10</sup>1F<sup>8</sup> with 13 12c-2e skeleton bonds, are the best known superatoms in boron chemistry due to their superb chemical stabilities [4–8]. All the seventeen bulk boron allotropes experimentally known to date, such as  $\alpha$ -B<sub>12</sub>,  $\gamma$ -B<sub>28</sub>,  $\beta$ -B<sub>106</sub>, and T-B<sub>192</sub>, are composed of icosahedral B<sub>12</sub> cages which in most cases are accompanied by certain numbers of boron atoms as interstitial atoms [9–11]. The simplest  $\alpha$ -rhombohedral boron ( $\alpha$ -B<sub>12</sub>) contains an icosahedral B<sub>12</sub> unit cell in  $D_{3d}$  symmetry following the  $n + 1$

Wade's rule [9, 12], while the unit cell of  $\gamma$ -orthorhombic B<sub>28</sub> ( $\gamma$ -B<sub>28</sub>) ((B<sub>12</sub>-B<sub>2</sub>)<sub>2</sub>) is composed of two icosahedral B<sub>12</sub> building blocks with two B–B interstitial dumbbells lying outside the B<sub>12</sub> cages [11, 13]. The most typical boron carbide B<sub>4</sub>C (CB<sub>11</sub>-CBC) experimentally characterized by annular bright-field (ABF) scanning transmission electron microscopy (STEM) contains a B<sub>11</sub>C icosahedron with a linear C–B–C interstitial chain in each unit cell [14].

Two-dimensional (2D) boron nanomaterials have attracted considerable attention in both experiments and theory in the past two decades [15–18]. Both atomically thin monolayer borophenes and bilayer borophenes have been synthesized by molecular beam epitaxy (MBE) experiments on Cu(111) and Ag(111) substrates which both turned out to be metallic in nature [19–22]. Monolayer 2D  $\gamma$ -B<sub>28</sub> films synthesized on copper (Cu) foils through chemical vapor deposition (CVD) consist of icosahedral B<sub>12</sub> cages and B–B interstitial dumbbells [23]. Freestanding few-layered  $\alpha$ -rhombohedral boron nanosheets have been achieved in a facile probe ultrasonic approach [24]. Based on semiconductor  $\alpha$ -B<sub>12</sub>, a series of 2D icosahedral boron sheets with icosahedral B<sub>12</sub> as building blocks have been predicted by first-principles theory

Received: November 20, 2024; Revised: January 14, 2025

Accepted: February 6, 2025

 Address correspondence to [lisidian@sxu.edu.cn](mailto:lisidian@sxu.edu.cn)

calculations [25, 26].  $\alpha$ -Boron (111) surface reconstructions have also been examined [27, 28]. Using icosahedron  $I_h$   $B_{12}H_{12}^{2-}$  and  $D_{5d}$   $1,12-C_2B_{10}H_{12}$  as building blocks, our group recently predicted at density functional theory (DFT) level a series of core-shell superpolyhedral boranes and carboranes, one-dimensional (1D)  $\alpha$ -rhombohedral borane nanowire  $B_{12}H_{10}$  ( $Pm\bar{3}m$ ), and 2D monolayer  $\alpha$ -rhombohedral borophane  $B_{12}H_6$  ( $P\bar{3}m1$ ), setting up a bottom-up strategy to form low-dimensional boron-based nanomaterials from their borane or carborane “seeds” via partial or complete dehydrogenations [29]. However, whether the 2D monolayer  $\alpha$ -rhombohedral borophane  $B_{12}H_6$  ( $P\bar{3}m1$ ) can be extended to form novel 2D few-layered  $\alpha$ -rhombohedral borophanes in a bottom-up approach still remains unknown. More importantly, if a general strategy can be established to form more complicated 2D few-layered borophanes and carborophanes and other experimentally known three-dimensional (3D) bulk boron allotropes like  $\gamma$ - $B_{28}$  and boron carbides like  $B_4C$  in bottom-up approaches remains a huge challenge to date in both experiments and theory.

Using the experimentally known aromatic icosahedral superatoms  $I_h$   $B_{12}H_{12}^{2-}$  and  $C_{5v}$   $B_{11}CH_{12}^-$  as precursors and based on extensive DFT calculations performed in this work, we predict herein bottom-up approaches to form the superatom-assembled 2D few-layered  $\alpha$ -rhombohedral borophanes  $(B_{12})_nH_6$  ( $\alpha$ -1–5) and  $(B_{12})_nH_2$  ( $\alpha$ -6–10), 2D  $\gamma$ -orthorhombic borophanes  $(B_{12}B_2)_nH_8$  ( $\gamma$ -1–5), and 2D carborophanes  $(CB_{11}-CBC)_nH_8$  ( $\sigma$ -1–5) ( $n = 1–5$ ) and the experimentally known 3D  $\alpha$ - $B_{12}$ ,  $\gamma$ - $B_{28}$ , and  $CB_{11}-CBC$  which are all composed of aromatic icosahedral  $B_{12}$  and  $CB_{11}$  building blocks via partial or complete dehydrogenations, respectively. The B-B dumbbells in  $\gamma$ -1–5 and C–B–C chains in  $\sigma$ -1–5 are found to serve as interstitial structural units in optimal configurations to help make the icosahedral  $B_{12}$  and  $CB_{11}$  building blocks match the  $n + 1$  Wade’s rule. These 2D few-layered borophanes and carborophanes all appear to be semiconductors in nature, with the few-layered carborophanes  $\sigma$ -3–5 ( $(CB_{11}-CBC)_nH_8$ ,  $n = 3–5$ ) possessing the band gaps of  $E_{gap} = 1.32–1.26$  eV well comparable with that of traditional silicon semiconductors. The high stabilities of these low-dimensional nanomaterials originate from the spherical aromaticity of their aromatic icosahedral  $B_{12}$  and  $CB_{11}$  building blocks which follow the universal superatomic electronic configuration of  $1S^21P^61D^{10}1F^8$ .

## 2 Theoretical procedures

Structural optimizations were performed on the concerned 2D and 3D crystals using the Vienna *ab initio* simulation package (VASP 5.4) [30, 31] at DFT level with the projector augmented wave (PAW) pseudopotential method [32, 33] and the PBE parametrization of generalized gradient approximation (GGA) [34]. The convergence criteria in electronic self-consistency and ionic residual forces are  $10^{-5}$  eV and  $10^{-3}$  eV/Å, respectively. A vacuum space of 15 Å was set to isolate neighboring periodic images and the cut-off energy is set as 500 eV. The k-point mesh was sampled with a resolution of  $2\pi \times 0.02$  Å<sup>-1</sup> [35]. The phonon dispersion curves along the high-symmetry lines were computed by the density-functional perturbation theory (DFPT) approach implemented in the phonopy package [36], where the precision convergence criteria for the total energy was set to  $10^{-9}$  eV to ensure the accuracy of calculations. The more accurate Heyd–Scuseria–Ernzerhof screened hybrid functional (HSE06) [37] was employed to calculate

the band structures and density of states (DOS) of the concerned crystals.

The dynamic stabilities of the concerned species were investigated by Born-Oppenheimer molecular dynamics (BOMD) simulations for 30 ps using the CP2K program [38], with the Goedecker–Teter–Hutter (GTH)-Perdew–Burke–Ernzerhof (PBE) pseudopotential and DZVP-MOLOPT-SR-GTH basis sets employed for B, C, and H. Chemical bonding analyses in 2D and 3D crystals were performed utilizing the solid-state adaptive natural density partitioning (SSAdNDP) program [39–41]. The results were visualized using the VMD 1.9.3 program [42].

## 3 Results and discussions

### 3.1 Structures and stability

As shown in Fig. 1, using the aromatic icosahedral  $B_{12}H_{12}^{2-}$  and  $CB_{11}H_{12}^-$  as precursors, bottom-up approaches can be established via partial dehydrogenations to form the 2D few-layered  $\alpha$ -rhombohedral borophanes  $(B_{12})_nH_6$  ( $\alpha$ -1–5) in (111) direction (Fig. 1(a)) and  $(B_{12})_nH_2$  ( $\alpha$ -6–10) in (001) direction (Fig. 1(b)), 2D  $\gamma$ -orthorhombic borophanes  $(B_{12}B_2)_nH_8$  ( $\gamma$ -1–5) in (001) direction (Fig. 1(c)), and carborophanes  $(CB_{11}-CBC)_nH_8$  ( $\sigma$ -1–5) in (010) direction (Fig. 1(d)), with the number of icosahedral layers changing between  $n = 1–5$ . The optimized 2D monolayer, bilayer, trilayer, tetralayer, and pentalayer crystals all turn out to be true minima of the systems without imaginary phonon frequencies, as clearly shown in Fig. 2 and Fig. S1 in the Electronic Supplementary Material (ESM). Extensive BOMD simulations performed at 1200 K in Fig. S2 in the ESM indicate that 2D monolayer  $B_{12}H_2$  ( $\alpha$ -6),  $B_{14}H_8$  ( $\gamma$ -1), and  $B_{12}C_3H_8$  ( $\sigma$ -1) are all dynamically stable, with the small average root-mean-square-deviations of RMSD = 0.11/0.11/0.10 Å and maximum bond length deviations of MAXD = 0.35/0.40/0.30 Å at 1200 K, respectively. Other few-layered borophanes and carborophanes and 3D  $\alpha$ - $B_{12}$ ,  $\gamma$ - $B_{28}$ , and  $CB_{11}-CBC$  exhibit similar dynamical stabilities at high temperatures (Fig. S2 in the ESM). Detailed PBE calculations indicate that these chemically stable 2D few-layered nanomaterials are also mechanically stable, with both their maximum and minimum Young’s modulus (N/m) increasing almost linearly with the number of icosahedral layers in the systems, as depicted in Fig. 3 and tabulated in Table S2 in the ESM. More profoundly, these few-layered 2D borophanes and carborophanes can be extended in vertical dimensions infinitely (with  $n = \infty$ ) via complete dehydrogenations to form the experimentally known 3D  $\alpha$ - $B_{12}$ ,  $\gamma$ - $B_{28}$ , and  $CB_{11}-CBC$  depicted at the end of each row, respectively, setting up a more general strategy to form low-dimensional boron-based nanomaterials based on their icosahedral borane or carborane “seeds”  $B_{12}H_{12}^{2-}$  and  $CB_{11}H_{12}^-$  in bottom-up approaches via partial or complete dehydrogenations.

The previously reported superatom-assembled 2D monolayer borophane  $B_{12}H_6$  ( $\alpha$ -1) ( $P\bar{3}m1$ ) in which each icosahedral  $D_{3d}$   $B_{12}$  cage is symmetrically surrounded by six equivalent  $B_{12}$  cages in the (111) direction of  $\alpha$ - $B_{12}$  [29] can be extended in vertical direction along the  $C_3$  axis of the unit cell by ABC stacking to form 2D bilayer  $B_{24}H_6$  ( $\alpha$ -2), trilayer  $B_{36}H_6$  ( $\alpha$ -3), tetralayer  $B_{48}H_6$  ( $\alpha$ -4), and pentalayer  $B_{60}H_6$  ( $\alpha$ -5), respectively, with the approximate lattice parameters of  $a = b \approx 4.87$  Å and  $\gamma = 120^\circ$ , as detailed in Fig. 1(a). The neighboring  $B_{12}$  layers in  $B_{24}H_6$  ( $\alpha$ -2),  $B_{36}H_6$  ( $\alpha$ -3),  $B_{48}H_6$  ( $\alpha$ -4), and  $B_{60}H_6$  ( $\alpha$ -5) are interconnected via typical interlayer B–B single bonds of about 1.66 Å, with the top and

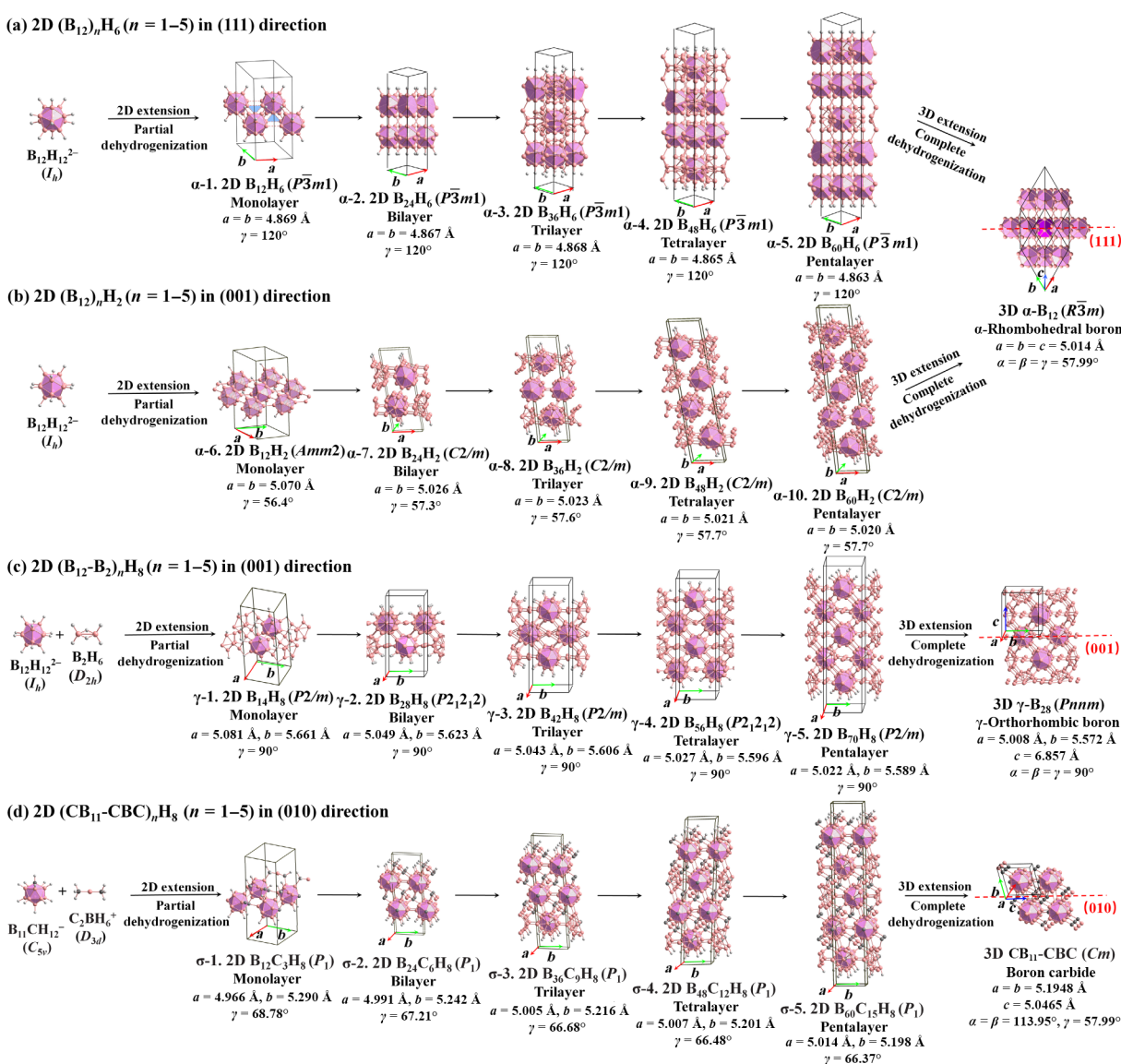


**Figure 1** Bottom-up approaches to form the superatom-assembled (a) 2D few-layered  $\alpha$ -rhombohedral borophanes  $(B_{12})_nH_6$  ( $\alpha$ -1–5) in (111) direction, (b)  $(B_{12})_nH_2$  ( $\alpha$ -6–10) in (001) direction, (c) 2D  $\gamma$ -orthorhombic borophanes  $(B_{12}-B_2)_nH_8$  ( $\gamma$ -1–5) in (001) direction, and (d)  $(CB_{11}-CBC)_nH_8$  ( $\sigma$ -1–5) in (010) direction ( $n = 1-5$ ) and 3D crystals  $\alpha$ - $B_{12}$ ,  $\gamma$ - $B_{28}$ , and  $CB_{11}-CBC$  using the aromatic icosahedral  $B_{12}H_{12}^{2-}$  and  $CB_{11}H_{12}^-$  as precursors at GGA-PBE level via partial or complete dehydrogenations, with the B–B dumbbells in  $\gamma$ -I–5 and C–B–C chains in  $\sigma$ -I–5 serving as interstitial structural units to help stabilize the icosahedral  $B_{12}$  and  $CB_{11}$  cages.

bottom  $B_{12}$  layers symmetrically saturated by six B–H terminal bonds in each unit cell. The 2D  $B_{12}H_6$  ( $\alpha$ -1),  $B_{12}H_6$  ( $\alpha$ -2),  $B_{36}H_6$  ( $\alpha$ -3),  $B_{48}H_6$  ( $\alpha$ -4), and  $B_{60}H_6$  ( $\alpha$ -5) in the same space group of  $P\bar{3}m1$  all turn out to be semiconductors in nature with the decreasing band gaps of  $E_{\text{gap}} = 2.25, 2.15, 2.00, 1.92,$  and  $1.89$  eV (Table S1 in the ESM and Fig. 3), respectively. As indicated in Fig. 2(a), the band gaps of the 2D few-layered  $\alpha$ -rhombohedral borophanes  $(B_{12})_nH_6$  ( $\alpha$ -1–5) decrease monotonically with the increasing numbers ( $n$ ) of  $B_{12}$  layers in the systems, approaching to the band gap of  $E_{\text{gap}} = 1.85$  eV in 3D  $\alpha$ - $B_{12}$  gradually when  $n = \infty$ . Projected densities of states (PDOS) analyses in Fig. 2 indicate B 2p orbitals dominate the total densities of states of all the concerned 2D few-layered structures.

Figure 1(b) shows the optimized structure of 2D monolayer  $\alpha$ -rhombohedral borophane  $B_{12}H_2$  ( $\alpha$ -6) ( $Amm2$ ) obtained in the (001) direction of 3D  $\alpha$ - $B_{12}$  with the optimized lattice parameters of  $a = b = 5.070 \text{ \AA}$  and  $\gamma = 56.4^\circ$ . Each  $C_{2v}$   $B_{12}H_2$  unit in it contains two terminal B–H bonds symmetrically distributed on the top and

bottom of the  $B_{12}$  cage. It is a semiconductor with the calculated indirect band gap of  $E_{\text{gap}} = 1.93$  eV (Fig. 2(a)). The 2D monolayer  $\alpha$ -rhombohedral  $B_{12}H_2$  can be extended in vertical direction to form the bilayer  $B_{24}H_2$  ( $C2/m$ ) ( $\alpha$ -7), trilayer  $B_{36}H_2$  ( $C2/m$ ) ( $\alpha$ -8), tetralayer  $B_{48}H_2$  ( $C2/m$ ) ( $\alpha$ -9), and pentalayer  $B_{60}H_2$  ( $C2/m$ ) ( $\alpha$ -10) which all appear to be semiconductors with the decreasing band gaps of  $E_{\text{gap}} = 1.84, 1.62, 1.59,$  and  $1.50$  eV (Table S1 in the ESM and Fig. 3), respectively, approaching to the band gap (1.21 eV) of silicon gradually. The optimized hexalayer  $B_{72}H_2$  ( $C2/m$ ) ( $\alpha$ -11) has a small band gap of  $E_{\text{gap}} = 1.46$  eV. These 2D multilayer  $\alpha$ -rhombohedral borophanes all turn out to have obviously narrower band gaps than that (2.25 eV) of the previously reported 2D monolayer  $B_{12}H_6$  ( $\alpha$ -1) [29].

The more complicated 2D few-layered  $\gamma$ -orthorhombic borophanes  $(B_{14})_nH_8$  ( $n = 1-5$ ) ( $\gamma$ -1–5) based on the structural motif of 3D  $\gamma$ - $B_{28}$  are depicted in Fig. 1(c). Using  $I_h$   $B_{12}H_{12}^{2-}$  and  $D_{2h}$   $B_2H_6$  as precursors, the 2D monolayer  $\gamma$ -orthorhombic borophane

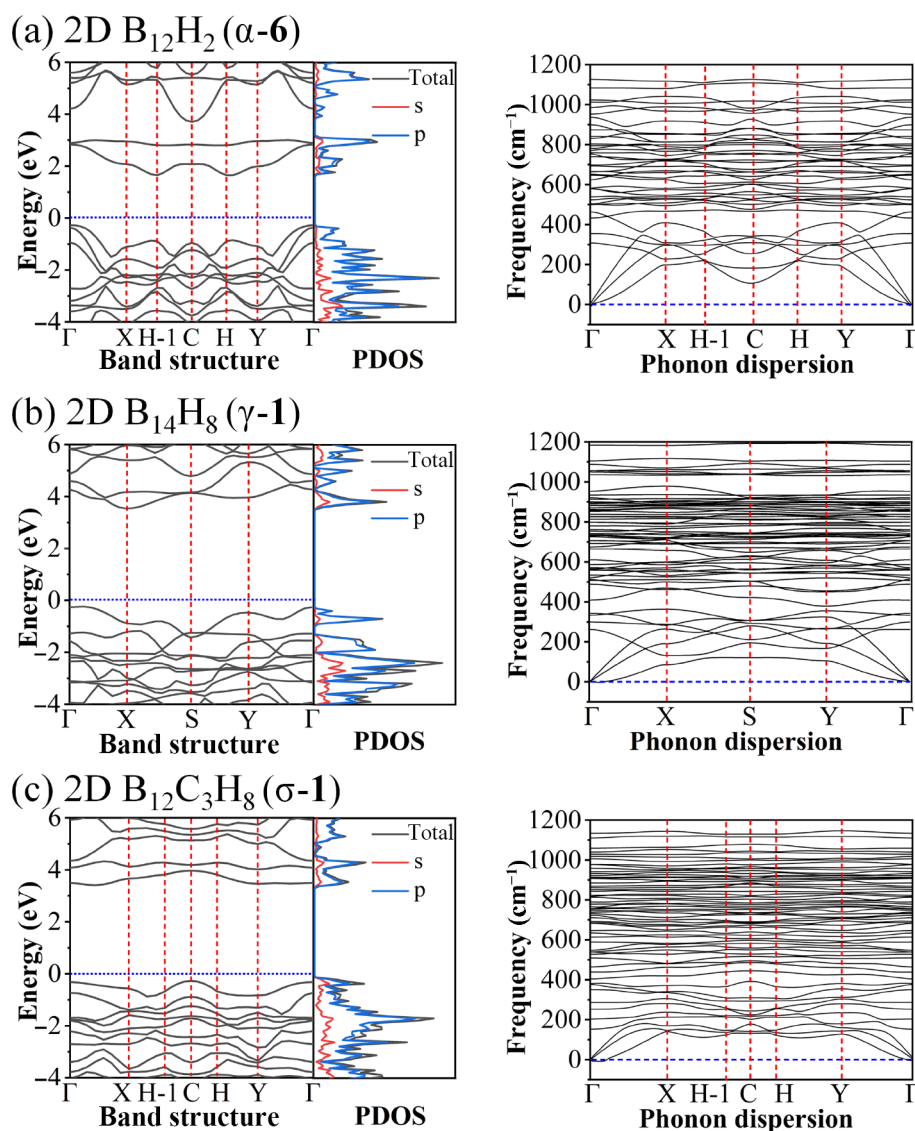


**Figure 2** Calculated band structures, projected densities of states (PDOS), and phonon dispersion spectra of 2D monolayer (a)  $\alpha$ -rhombohedral borophane  $B_{12}H_2$  ( $\alpha$ -6), (b)  $\gamma$ -orthorhombic borophane  $B_{14}H_8$  ( $\gamma$ -1), and (c) carborophane  $B_{12}C_3H_8$  ( $\sigma$ -1) with the band gaps of  $E_{\text{gap}} = 1.93, 3.78,$  and  $3.68$  eV at GGA-HSE06 level, respectively.

$B_{14}H_8$  ( $P2/m$ ) ( $\gamma$ -1) can be obtained by partial dehydrogenations in the (001) direction of  $\gamma$ - $B_{28}$ .  $B_{14}H_8$  ( $\gamma$ -1) possesses one icosahedral  $B_{12}$  cage and one interstitial B-B dumbbell in each unit, with the optimized lattice parameters of  $a = 5.081$  Å,  $b = 5.661$  Å, and  $\gamma = 90^\circ$ . It contains four B-H terminal bonds and four B-H-B bridging bonds in each unit cell to make the system satisfy its optimal bonding requirements. 2D  $B_{14}H_8$  ( $P2/m$ ) ( $\gamma$ -1) can be extended in vertical direction by AB stacking to form the 2D  $\gamma$ -orthorhombic bilayer  $B_{28}H_8$  ( $P2_12_2$ ) ( $\gamma$ -2), trilayer  $B_{42}H_8$  ( $P2/m$ ) ( $\gamma$ -3), tetralayer  $B_{56}H_8$  ( $P2_12_12$ ) ( $\gamma$ -4), and pentalayer  $B_{70}H_8$  ( $P2/m$ ) ( $\gamma$ -5) with the interlayer B-B  $\sigma$  bonds of about 1.60 Å. The 2D  $\gamma$ -orthorhombic borophane series  $(B_{14})_nH_8$  all turn out to be semiconductors in nature with the calculated band gaps of  $E_{\text{gap}} = 3.78, 3.17, 2.84, 2.78,$  and  $2.6$  eV for  $n = 1, 2, 3, 4,$  and  $5$  (Table S1 in the ESM), respectively. Their band gaps also decrease monotonically with the increasing numbers of  $B_{12}$  layers (Fig. 3(c)), gradually approaching to the indirect bandgap of  $E_{\text{gap}} = 2.35$  eV calculated for bulk boron  $\gamma$ - $B_{28}$  at the same theoretical level.

The most complicated 2D few-layered carborophanes  $(CB_{11}\text{-}CBC)_nH_8$  ( $n = 1\text{-}5$ ) based on structural pattern of 3D  $CB_{11}\text{-}CBC$  are

depicted in Fig. 1(d) which contains an icosahedral  $CB_{11}$  cage and an interstitial C-B-C chain in each unit cell. Using the aromatic icosahedral carborane  $C_{5v}$ ,  $CB_{11}H_{12}^-$  and linear  $D_{3d}$   $C_2BH_6^+$  chain as precursors, the 2D monolayer carborophane  $B_{12}C_3H_8$  ( $P1$ ) ( $\sigma$ -1) can be achieved in the (001) direction of 3D  $CB_{11}\text{-}CBC$  by partial dehydrogenations. It contains five B-H terminal bonds and three C-H terminal bonds to make the system satisfy its optimal bonding requirements, with the optimized lattice parameters of  $a = 4.966$  Å,  $b = 5.290$  Å, and  $\gamma = 68.78^\circ$  and the band gap of  $E_{\text{gap}} = 3.68$  eV. It can be extended in vertical direction to form the bilayer  $B_{24}C_6H_8$  ( $P1$ ) ( $\sigma$ -2), trilayer  $B_{36}C_9H_8$  ( $P1$ ) ( $\sigma$ -3), tetralayer  $B_{48}C_{12}H_8$  ( $P1$ ) ( $\sigma$ -4), and pentalayer  $B_{60}C_{15}H_8$  ( $P1$ ) ( $\sigma$ -5) which, as semiconductors in nature, have the calculated band gaps of  $E_{\text{gap}} = 1.74, 1.32, 1.29,$  and  $1.26$  eV, respectively. More intriguingly, the few-layered carborophanes  $\sigma$ -3-5  $(CB_{11}\text{-}CBC)_nH_8$  ( $n = 3\text{-}5$ ) obtained herein with band gaps between  $E_{\text{gap}} = 1.32\text{-}1.26$  eV all appear to be well compatible with traditional silicon semiconductors with  $E_{\text{gap}} = 1.21$  eV in band gaps.

Figure 3 clearly indicates that the overall cohesive energies per unit cell of 2D few-layered  $(B_{12})_nH_6$  ( $\alpha$ -1-5) (a),  $(B_{12})_nH_2$  ( $\alpha$ -6-10)

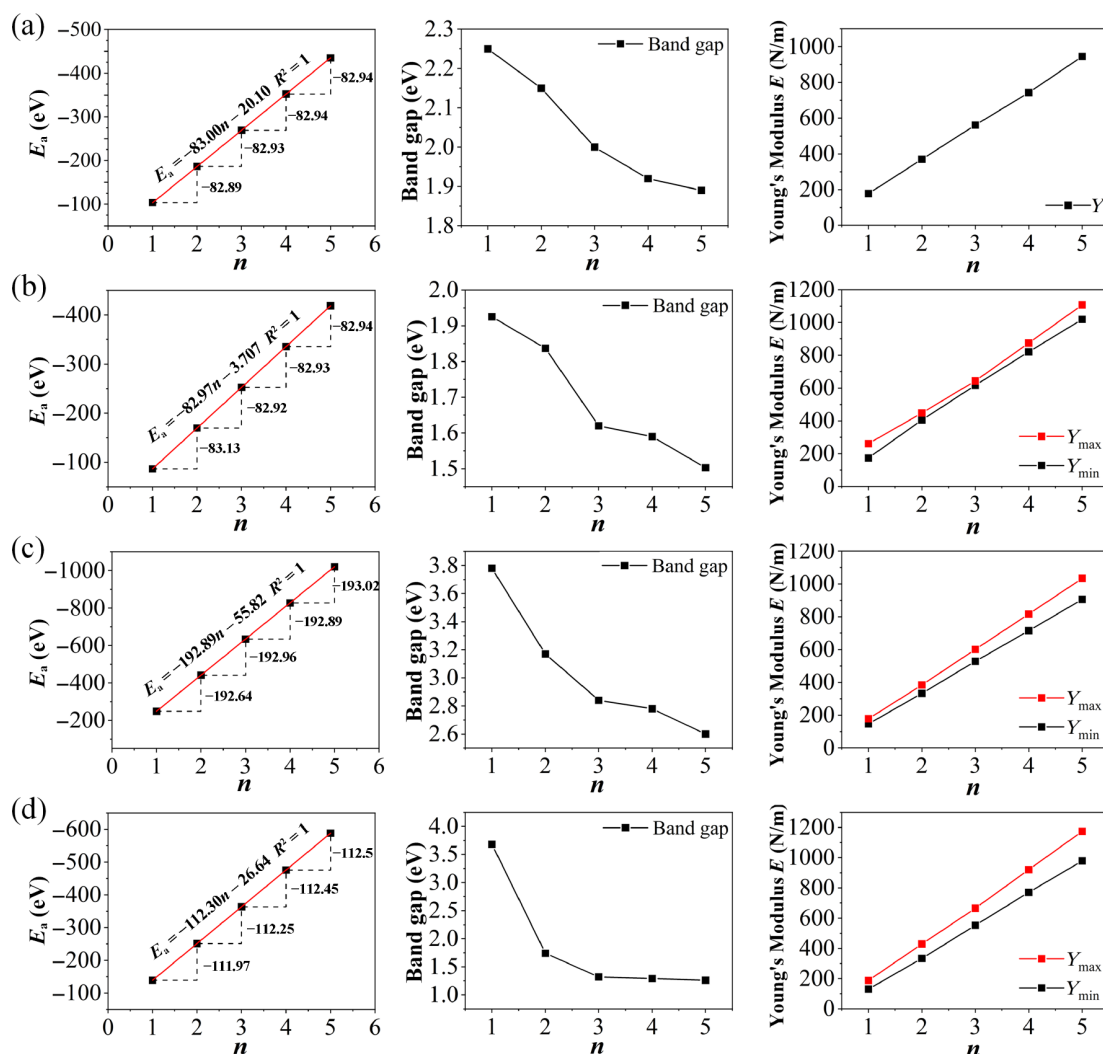


**Figure 3** Evolution of the unit-cell cohesive energies  $E_a$  (in eV), band gaps  $E_{\text{gap}}$  (in eV), and the maximum ( $Y_{\text{max}}$ ) and minimum ( $Y_{\text{min}}$ ) Young's modulus (in N/m) of the 2D few-layered (a)  $\alpha$ -rhombohedral borophanes  $(\text{B}_{12})_n\text{H}_6$  ( $n = 1-5$ ,  $\alpha$ -1-5), (b)  $\alpha$ -rhombohedral borophanes  $(\text{B}_{12})_n\text{H}_2$  ( $n = 1-5$ ,  $\alpha$ -6-10), (c)  $\gamma$ -orthorhombic borophanes  $(\text{B}_{14})_n\text{H}_8$  ( $n = 1-5$ ,  $\gamma$ -1-5), and (d) carborophanes  $(\text{B}_{12})_n\text{C}_3\text{H}_8$  ( $n = 1-5$ ,  $\sigma$ -1-5).

(b),  $(\text{B}_{14})_n\text{H}_8$  ( $\gamma$ -1-5) (c), and  $(\text{CB}_{11}\text{-CBC})_n\text{H}_8$  ( $\sigma$ -1-5) ( $n = 1-5$ ) increase almost perfectly linearly with the increasing numbers ( $n$ ) of icosahedral layers in the systems. More intriguingly, the slopes of the linear relationships of 83.00, 82.97, 192.89, and 112.30 eV which represent the average cohesive energy per unit cell per icosahedral layer well correspond to the cohesive energy per unit cell of  $\alpha$ - $\text{B}_{12}$  ( $-82.94$  eV),  $\gamma$ - $\text{B}_{28}$  ( $-192.98$  eV), and  $\text{CB}_{11}\text{-CBC}$  ( $-112.58$  eV) at the same theoretical level, respectively, in which the unit cells of the  $(\text{B}_{14})_n\text{H}_8$  ( $\gamma$ -1-5) are doubled in size to match the unit cell of  $\gamma$ - $\text{B}_{28}$ .

### 3.2 Bonding pattern analyses

To better comprehend the bottom-up approaches presented in this work, detailed AdNDP and SSAdNDP bonding analyses [40, 41] are performed on the much concerned 2D monolayer and bilayer species and 3D crystals to unveil both the localized and delocalized bonds in them in Fig. 4. The spherically aromatic icosahedral  $\text{B}_{12}\text{H}_{12}^{2-}$  and  $\text{C}_{5v}\text{B}_{11}\text{CH}_{12}^{-}$  are well known to follow the  $n + 1$  Wade's rule ( $n = 12$ ) with the superatomic electronic configuration of  $1\text{S}^21\text{P}^61\text{D}^{10}1\text{F}^8$ , as shown in Fig. S3 in the ESM.

As indicated in Fig. 4(a), each  $\text{B}_{12}$  icosahedron in monolayer  $\text{B}_{12}\text{H}_2$  ( $\alpha$ -6) participates in 2 2c-2e B-H terminal bonds on the top

and bottom of the icosahedral  $\text{B}_{12}$  cage and 8 2c-2e B-B bonds with six neighboring  $\text{B}_{12}$  cages around it, in the overall symmetry of  $\text{C}_{2v}$ . The remaining 26 valence electrons of the  $\text{B}_{12}$  icosahedron forms 13 12c-2e skeleton bonds totally delocalized over the over the  $\text{B}_{12}$  cage, including 1 S-type bond, 3 P-type bonds, 5 D-type bonds, and 4 F-type bonds in the aromatic superatomic electronic configuration of  $1\text{S}^21\text{P}^61\text{D}^{10}1\text{F}^8$ . Figure 4(b) indicates that the top  $\text{B}_{12}\text{H}$  unit in 2D bilayer  $\text{B}_{24}\text{H}_2$  ( $\alpha$ -7) participates in 1 2c-2e B-H bond, 7 2c-2e B-B bonds, and 3 3c-2e B-B-B bonds, with each  $\text{B}_{12}$  cage again matching the electronic configuration of  $1\text{S}^21\text{P}^61\text{D}^{10}1\text{F}^8$ . Similar bonding patterns exist in trilayer  $\text{B}_{36}\text{H}_2$  ( $\alpha$ -8), tetralayer  $\text{B}_{48}\text{H}_2$  ( $\alpha$ -9), and pentalayer  $\text{B}_{60}\text{H}_2$  ( $\alpha$ -10). Such bonding patterns of the few-layered  $\alpha$ -rhombohedral borophanes  $(\text{B}_{12})_n\text{H}_2$  ( $n = 1-5$ ) are well in line with that of 3D  $\alpha$ - $\text{B}_{12}$  in which each  $\text{B}_{12}$  unit cell participates in 6 2c-2e B-B on the top and bottom and 6 3c-2e B-B-B bonds around it in the overall symmetry of  $\text{D}_{3d}$  with the remaining 26 electrons following electronic configuration of  $1\text{S}^21\text{P}^61\text{D}^{10}1\text{F}^8$ , as clearly shown in Fig. 4(c). The unique arrangement of the 6 3c-2e B-B-B bonds in which each B atom contributes 2/3 valence electron helps to make each  $\text{D}_{3d}$   $\text{B}_{12}$  unit cell match the Wade's rule.

As demonstrated in Fig. 4(d), each  $\text{B}_{12}$  cage in monolayer  $\text{B}_{14}\text{H}_8$

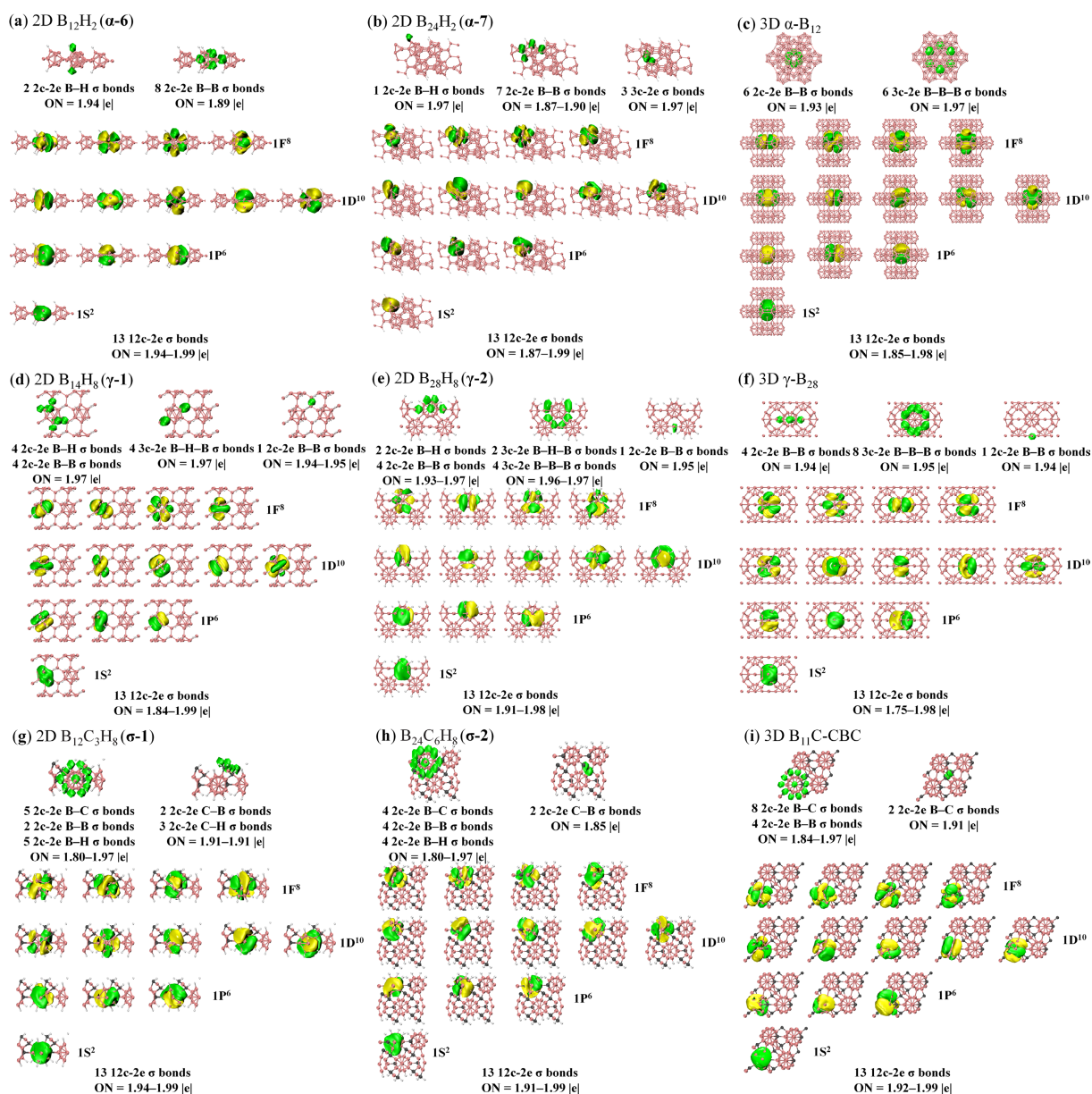


**Figure 4** SSAdNDP bonding patterns of 2D (a) monolayer  $B_{12}H_2$  ( $\alpha$ -6), (b) bilayer  $B_{24}H_2$  ( $\alpha$ -7), (d) monolayer  $B_{14}H_8$  ( $\gamma$ -1), (e) bilayer  $B_{28}H_8$  ( $\gamma$ -2), (g) monolayer  $B_{12}C_3H_8$  ( $\sigma$ -1), and (h) bilayer  $B_{24}C_6H_8$  ( $\sigma$ -2), compared with their corresponding 3D crystals (c)  $\alpha$ - $B_{12}$ , (f)  $\gamma$ - $B_{28}$ , and (i)  $B_{11}C$ -CBC.

( $\gamma$ -1) participates in 4 2c-2e B-H terminal bonds on the top and bottom, 4 2c-2e B-B bonds with neighboring  $B_{12}$  cages and B-B dumbbells, and 4 3c-2e B-H-B bridging bonds with neighboring B-B dumbbells in the overall symmetry of  $C_{2h}$ , with the remaining 26 electrons follow the superatomic configuration of  $1S^21P^61D^{10}1F^8$ . It is the 4 3c-2e B-H-B bridging bonds in which each B contributes half a valence electron that helps make the  $B_{12}$  cage match the Wade's rule. The 2D bilayer  $B_{28}H_8$  ( $\gamma$ -2) has a similar bonding pattern (Fig. 4(e)). Interestingly, as shown in Fig. 4(f), each  $B_{12}$  icosahedron in 3D  $\gamma$ - $B_{28}$  participates in 4 2c-2e B-B bonds with two neighboring  $B_{12}$  cages and two neighboring B-B dumbbells and 8 3c-2e B-B-B bonds with the surrounding  $B_{12}$  cages and B-B dumbbells. The  $B_{12}$  unit thus again follows the Wade's rule in electronic configuration of  $1S^21P^61D^{10}1F^8$ . We address here that it is the 8 3c-2e B-B-B bonds with the surrounding  $B_{12}$  cages and interstitial B-B dumbbells that help make each  $B_{12}$  icosahedron in 3D  $\gamma$ - $B_{28}$  match the Wade's rule.

Interestingly and intriguingly, Fig. 5(g) indicates that each interstitial C-B-C chain in 2D monolayer  $B_{12}C_3H_8$  ( $\sigma$ -1) participates in 5 2c-2e B-C single bonds and 3 2c-2e C-H single bonds, it therefore has one extra valence electron to donate, while the  $CB_{11}$  icosahedron forms 12 2c-2e single bonds with its neighbors, with one-electron's deficiency to match the Wade's rule. The C-B-C chain in crystal thus donates one extra valence electron to the neighboring  $CB_{11}$  icosahedron to make it satisfy the Wade's  $n + 1$  rule with the electronic configuration of  $1S^21P^61D^{10}1F^8$ . Similar situation happens to bilayer carborophanes  $B_{24}C_6H_8$  ( $\sigma$ -2) which also involves an electron transfer from the C-B-C chain to the  $CB_{11}$  cage (Fig. 4(h)). Similarly, the positively charged  $[C-B-C]^+$  interstitial chain in 3D  $CB_{11}$ -CBC participates in 2 2c-2e B-C single bonds within the C-B-C chain and 6 C-B single bonds with the  $CB_{11}$  cages around it, while the negatively charged  $[CB_{11}]^-$  icosahedron which forms 8 C-B bonds and 4 2c-2e B-B bonds with its neighbors also turns out to follow the electron

configuration of  $1S^21P^61D^{10}1F^8$  (Fig. 4(i)). The 3D  $CB_{11}$ -CBC crystal is therefore a charge-transfer complex  $[CB_{11}]^--[CBC]^+$  in nature. It is the charge transfer that makes the  $CB_{11}$  cage match the Wade's rule to help stabilize the system.

## 4 Conclusions

In summary, extensive DFT calculations performed in this work present four bottom-up approaches to form the concerned superatom-assembled 2D few-layered borophanes and carborophanes and their corresponding 3D crystals based on aromatic icosahedral  $B_{12}$  and  $CB_{11}$ , with the B-B dumbbells and C-B-C chains serving as interstitial structural units to help make the icosahedra in the systems match the Wade's rule. The icosahedral  $B_{12}$  and  $CB_{11}$  cages in these highly stable 2D and 3D semiconductors based on the structural motifs of the experimentally known 3D  $\alpha$ - $B_{12}$ ,  $\gamma$ - $B_{28}$ , and  $CB_{11}$ -CBC all turn out to have the universal electronic configuration of  $1S^21P^61D^{10}1F^8$ , rendering local spherical aromaticity and overall high stability to the systems. Such chemically and mechanically stable low-dimensional boron-based nanomaterials are possible to be realized in future experiments with suitable dehydrogenation catalysts which deserve more extensive and in-depth explorations. More joint theoretical and experimental investigations are invited to establish a general strategy to form novel 1D and 2D boron-based nanomaterials and all the experimentally known 3D bulk boron allotropes and carbide crystals in bottom-up approaches matching certain electron counting rules.

**Electronic Supplementary Material:** Supplementary material (crystal structure information, Young's modulus, band structures, projected densities of states, phonon dispersion spectra, and molecular dynamics simulations in Tables S1–S3 and Figs. S1–S3) is available in the online version of this article at <https://doi.org/10.26599/NR.2025.94907288>.

## Data availability

All data needed to support the conclusions in the paper are presented in the manuscript and the Electronic Supplementary Material. Additional data related to this paper may be requested from the corresponding author upon request.

## Acknowledgments

This work was supported by the National Natural Science Foundation of China (No. 22373061).

## Declaration of competing interest

All the contributing authors report no conflict of interests in this work.

## Author contribution statement

Q.-Q. Y.: Data curation, validation, writing manuscript, W.-Y. Z.: Validation. Y.-W. M.: Validation. S.-D. L.: Project administration, funding acquisition, writing and finalizing manuscript. All the authors have approved the final manuscript.

## Use of AI statement

None.

## References

- [1] Cotton, F. A.; Wilkinson, G.; Murillo, C. A.; Bochmann, M. *Advanced Inorganic Chemistry*; 6th ed. Wiley: New York, 1999.
- [2] Wang, L. S. Photoelectron spectroscopy of size-selected boron clusters: From planar structures to borophenes and borospherenes. *Int. Rev. Phys. Chem.* **2016**, *35*, 69–142.
- [3] Jian, T.; Chen, X. N.; Li, S. D.; Boldyrev, A. I.; Li, J.; Wang, L. S. Probing the structures and bonding of size-selected boron and doped-boron clusters. *Chem. Soc. Rev.* **2019**, *48*, 3550–3591.
- [4] Sivaev, I. B.; Bregadze, V. I.; Sjöberg, S. Chemistry of closedodecaborate anion  $[B_{12}H_{12}]^{2-}$ : A review. *Collect. Czech. Chem. Commun.* **2002**, *67*, 679–727.
- [5] Hosmane, N. S. *Boron Science: New Technologies and Applications*; CRC Press: Boca Raton, 2012.
- [6] Grimes, R. N. *Carboranes*; 3rd ed. Elsevier: Amsterdam, 2016.
- [7] Wade, K. The structural significance of the number of skeletal bonding electron-pairs in carboranes, the higher boranes and borane anions, and various transition-metal carbonyl cluster compounds. *J. Chem. Soc. D* **1971**, 792–793.
- [8] Pitochelli, A. R.; Hawthorne, F. M. The isolation of the icosahedral  $B_{12}H_{12}^{2-}$  ion. *J. Am. Chem. Soc.* **1960**, *82*, 3228–3229.
- [9] McCarty, L. V.; Kasper, J. S.; Horn, F. H.; Decker, B. F.; Newkirk, A. E. A new crystalline modification of boron. *J. Am. Chem. Soc.* **1958**, *80*, 2592–2592.
- [10] Albert, B.; Hillebrecht, H. Boron: Elementary challenge for experimenters and theoreticians. *Angew. Chem., Int. Ed.* **2009**, *48*, 8640–8668.
- [11] Oganov, A. R.; Chen, J. H.; Gatti, C.; Ma, Y. Z.; Ma, Y. M.; Glass, C. W.; Liu, Z. X.; Yu, T.; Kurakevych, O. O.; Solozhenko, V. L. Ionic high-pressure form of elemental boron. *Nature* **2009**, *457*, 863–867.
- [12] Fujimori, M.; Nakata, T.; Nakayama, T.; Nishibori, E.; Kimura, K.; Takata, M.; Sakata, M. Peculiar covalent bonds in  $\alpha$ -rhombohedral boron. *Phys. Rev. Lett.* **1999**, *82*, 4452–4455.
- [13] Zarechnaya, E. Y.; Dubrovinsky, L.; Dubrovinskaia, N.; Filinchuk, Y.; Chernyshov, D.; Dmitriev, V.; Miyajima, N.; El Goresy, A.; Braun, H. F.; Van Smaalen, S. et al. Superhard semiconducting optically transparent high pressure phase of boron. *Phys. Rev. Lett.* **2009**, *102*, 185501.
- [14] Reddy, K. M.; Liu, P.; Hirata, A.; Fujita, T.; Chen, M. W. Atomic structure of amorphous shear bands in boron carbide. *Nat. Commun.* **2013**, *4*, 2483.
- [15] Piazza, Z. A.; Hu, H. S.; Li, W. L.; Zhao, Y. F.; Li, J.; Wang, L. S. Planar hexagonal  $B_{36}$  as a potential basis for extended single-atom layer boron sheets. *Nat. Commun.* **2014**, *5*, 3113.
- [16] Li, D. F.; Gao, J. F.; Cheng, P.; He, J.; Yin, Y. X.; Hu, Y.; Chen, L.; Cheng, Y.; Zhao, J. J. 2D boron sheets: Structure, growth, and electronic and thermal transport properties. *Adv. Funct. Mater.* **2020**, *30*, 1904349.
- [17] Yang, R.; Sun, M. T. Borophenes: Monolayer, bilayer and heterostructures. *J. Mater. Chem. C* **2023**, *11*, 6834–6846.
- [18] Gupta, G. H.; Kadakia, S.; Agiwal, D.; Keshari, T.; Kumar, S. Borophene nanomaterials: Synthesis and applications in biosensors. *Mater. Adv.* **2024**, *5*, 1803–1816.
- [19] Mannix, A. J.; Zhou, X. F.; Kiraly, B.; Wood, J. D.; Alducin, D.; Myers, B. D.; Liu, X. L.; Fisher, B. L.; Santiago, U.; Guest, J. R. et al. Synthesis of borophenes: Anisotropic, two-dimensional boron polymorphs. *Science* **2015**, *350*, 1513–1516.
- [20] Feng, B. J.; Zhang, J.; Zhong, Q.; Li, W. B.; Li, S.; Li, H.; Cheng, P.; Meng, S.; Chen, L.; Wu, K. H. Experimental realization of two-dimensional boron sheets. *Nat. Chem.* **2016**, *8*, 563–568.
- [21] Liu, X. L.; Li, Q. C.; Ruan, Q. Y.; Rahn, M. S.; Yakobson, B. I.; Hersam, M. C. Borophene synthesis beyond the single-atomic-layer limit. *Nat. Mater.* **2022**, *21*, 35–40.

- [22] Chen, C. Y.; Lv, H. F.; Zhang, P.; Zhuo, Z. W.; Wang, Y.; Ma, C.; Li, W. B.; Wang, X. G.; Feng, B. J.; Cheng, P. et al. Synthesis of bilayer borophene. *Nat. Chem.* **2022**, *14*, 25–31.
- [23] Tai, G. A.; Hu, T. S.; Zhou, Y. G.; Wang, X. F.; Kong, J. Z.; Zeng, T.; You, Y. C.; Wang, Q. Synthesis of atomically thin boron films on copper foils. *Angew. Chem.* **2015**, *127*, 15693–15697.
- [24] Liang, X. C.; Hao, J. Q.; Zhang, P. Y.; Hou, C.; Tai, G. A. Freestanding  $\alpha$ -rhombohedral borophene nanosheets: Preparation and memory device application. *Nanotechnology* **2022**, *33*, 505601.
- [25] Kah, C. B.; Yu, M.; Tandy, P.; Jayanthi, C. S.; Wu, S. Y. Low-dimensional boron structures based on icosahedron B<sub>12</sub>. *Nanotechnology* **2015**, *26*, 405701.
- [26] Yu, X.; Zhou, T. G.; Zhao, Y. C.; Lu, F.; Zhang, X. M.; Liu, G. D.; Gou, H. Y.; Zurek, E.; Luo, X. G. Surface magnetism in pristine  $\alpha$  rhombohedral boron and intersurface exchange coupling mechanism of boron icosahedra. *J. Phys. Chem. Lett.* **2021**, *12*, 6812–6817.
- [27] Amsler, M.; Botti, S.; Marques, M. A. L.; Goedecker, S. Conducting boron sheets formed by the reconstruction of the  $\alpha$ -boron (111) surface. *Phys. Rev. Lett.* **2013**, *111*, 136101.
- [28] Zhou, X. F.; Oganov, A. R.; Shao, X.; Zhu, Q.; Wang, H. T. Unexpected reconstruction of the  $\alpha$ -boron (111) surface. *Phys. Rev. Lett.* **2014**, *113*, 176101.
- [29] Yan, Q. Q.; Wei, Y. F.; Chen, Q.; Mu, Y. W.; Li, S. D. Superatom-assembled boranes, carboranes, and low-dimensional boron nanomaterials based on aromatic icosahedral B<sub>12</sub> and C<sub>2</sub>B<sub>10</sub>. *Nano Res.* **2024**, *17*, 6734–6740.
- [30] Kresse, G.; Furthmüller, J. Efficient iterative schemes for *ab initio* total-energy calculations using a plane-wave basis set. *Phys. Rev. B* **1996**, *54*, 11169–11186.
- [31] Kresse, G.; Furthmüller, J. Efficiency of *ab-initio* total energy calculations for metals and semiconductors using a plane-wave basis set. *Comput. Mater. Sci.* **1996**, *6*, 15–50.
- [32] Blöchl, P. E. Projector augmented-wave method. *Phys. Rev. B* **1994**, *50*, 17953–17979.
- [33] Kresse, G.; Joubert, D. From ultrasoft pseudopotentials to the projector augmented-wave method. *Phys. Rev. B* **1999**, *59*, 1758–1775.
- [34] Perdew, J. P.; Burke, K.; Ernzerhof, M. Generalized gradient approximation made simple. *Phys. Rev. Lett.* **1996**, *77*, 3865–3869.
- [35] Monkhorst, H. J.; Pack, J. D. Special points for Brillouin-zone integrations. *Phys. Rev. B* **1976**, *13*, 5188–5192.
- [36] Togo, A.; Oba, F.; Tanaka, I. First-principles calculations of the ferroelastic transition between rutile-type and CaCl<sub>2</sub>-type SiO<sub>2</sub> at high pressures. *Phys. Rev. B* **2008**, *78*, 134106.
- [37] Heyd, J.; Scuseria, G. E.; Ernzerhof, M. Hybrid functionals based on a screened Coulomb potential. *J. Chem. Phys.* **2003**, *118*, 8207–8215.
- [38] VandeVondele, J.; Krack, M.; Mohamed, F.; Parrinello, M.; Chassaing, T.; Hutter, J. Quickstep: Fast and accurate density functional calculations using a mixed Gaussian and plane waves approach. *Comput. Phys. Commun.* **2005**, *167*, 103–128.
- [39] Zubarev, D. Y.; Boldyrev, A. I. Comprehensive analysis of chemical bonding in boron clusters. *J. Comput. Chem.* **2007**, *28*, 251–268.
- [40] Zubarev, D. Y.; Boldyrev, A. I. Developing paradigms of chemical bonding: Adaptive natural density partitioning. *Phys. Chem. Chem. Phys.* **2008**, *10*, 5207–5217.
- [41] Galeev, T. R.; Dunnington, B. D.; Schmidt, J. R.; Boldyrev, A. I. Solid state adaptive natural density partitioning: A tool for deciphering multi-center bonding in periodic systems. *Phys. Chem. Chem. Phys.* **2013**, *15*, 5022–5029.
- [42] Humphrey, W.; Dalke, A.; Schulten, K. VMD: Visual molecular dynamics. *J. Mol. Graph.* **1996**, *14*, 33–38.



This is an open access article under the terms of the Creative Commons Attribution 4.0 International License (CC BY 4.0, <https://creativecommons.org/licenses/by/4.0/>).

© The Author(s) 2025. Published by Tsinghua University Press.